scientific reports

Check for updates

OPEN

Micro aluminum-air batteries for extended operational duration of small-scale quadrotors

Yanghang Huang[1]✉, Chenhao Wang[2], Haoxuan Lyu[3], Mark G. Allen[3]✉ & Sue Ann Bidstrup Allen[1]✉

Small-scale quadrotors, typically defined as centimeter-scale in size and tens of grams in weight, are increasingly being utilized in applications such as agricultural monitoring or search and rescue operations. These vehicles are typically powered with lithium-ion batteries. However, vehicle operational efficiency and capability are often compromised by the limited energy density of these batteries, resulting in short operational duration. This work explores a high-energy chemistry, aluminum-air (Al-air), as a power source to significantly extend the operational duration of small-scale quadrotors. Rapid corrosion of the aluminum anode in existing Al-air systems has been a barrier to adoption in applications where long-term operation is required. However, corrosion is less of a concern in the small-scale quadrotor application, where the battery is typically under continuous use over a short period of time. The electrochemical and packaging design of a micro-Al-air pouch cell battery is optimized for two operating points: an energy density of 325 $\frac{Wh}{kg_{battery}}$ above a power density of 500 $\frac{W}{kg_{battery}}$, and an energy density of 240 $\frac{Wh}{kg_{battery}}$ above a power density of 800 $\frac{W}{kg_{battery}}$, both of which far surpass the performance of equivalent commercial lithium-ion batteries. A 3D-printed small-scale quadrotor platform is used to evaluate flight duration. The micro Al-air battery delivers 13.1 min of flight time, compared to the 4.5 min of flight time provided by the commercial micro lithium-ion battery. This work demonstrates the feasibility of Al-air batteries that simultaneously possess sufficiently high power density to achieve small-scale quadrotor flight, and sufficiently high energy density to achieve extended duration of that flight.

The global drone market is growing at an unprecedented speed, and several forecasts predict that the market size could reach tens of billions by 2025[1]. The surge in drone technology prominence is attributable to its diverse applications set, including surveillance, aerial photography, environmental monitoring, and precision agriculture[2,3]. The need for drones with improved capabilities has led to the development of smaller and lighter platforms that can perform tasks with greater precision and efficiency[4]. Consequently, this evolution has spurred an interest in the development of small-scale quadrotors, which are typically centimeter-scale in size and weigh tens of grams; such advanced small-scale quadrotors can, for example, navigate through confined spaces[5–7]. Concurrently, this quadrotor miniaturization has highlighted the importance of on-board power sources, resulting in significant research and development efforts. In particular, the need to develop power sources that fit within the miniature quadrotor platform and simultaneously provide sufficient power and energy performance for both small-scale quadrotor takeoff and extended flight duration has emerged as a critical need in this field[8–10].

Electrochemical cells, or batteries (these terms will be used interchangeably in this work), are the typical power sources utilized for small-scale quadrotors. Among these batteries, Lithium-ion batteries (LIBs) have been a preferred power source, due to both LIB availability and scalability[11–13]. Despite these advantages, there is still a need to optimize the onboard power source with respect to two highly important design metrics: gravimetric energy density and gravimetric power density. The gravimetric energy density of the onboard power source determines the flight duration, while the liftoff and maneuverability of the small-scale quadrotor set a minimum requirement on the gravimetric power density of the onboard power source[14]. Micro-LIBs (mLIBs) can easily meet the power requirement of the small-scale quadrotor; however, the flight duration of the small-scale

[1]Chemical and Biomolecular Engineering, University of Pennsylvania, Philadelphia, PA 19104, USA. [2]Materials Science and Engineering, University of Pennsylvania, Philadelphia, PA 19104, USA. [3]Electrical and Systems Engineering, University of Pennsylvania, Philadelphia, PA 19104, USA. ✉email: yanghang@alumni.upenn.edu; mallen@seas.upenn.edu; sb3@seas.upenn.edu

quadrotor is limited by the mLIBs gravimetric energy density, especially at high power loads. The operational capability of small-scale quadrotors is often compromised by this resultant short operation duration.

Figure 1 (A) plots the energy density of commercial mLIBs as a function of the LIB mass, ranging from 0.04 g to over 40 g. The dataset is collected from the specification sheets of the manufacturers of commercial LIBs as well as values reported values in the literature[15–19]. Figure 1 (A) shows that when the battery size exceeds 10 g, no significant correlation between the cell size and energy density is observed. However, for batteries less than 10 g, the gravimetric energy density of the mLIB decreases as the battery size shrinks. Several factors contribute to this decline. As the size of the battery decreases, a more significant fraction of its total mass is dedicated to isolating the reactive components from the environment[20]. Such isolation is required because the electrolytes and electrodes of LIBs are not inherently stable under ambient conditions[21,22]. However, although these isolation materials have finite mass, they do not contribute to the electrochemical reactions that generate energy. For example, the packaging overhead (i.e., fraction of total cell mass attributable to the isolation package) for gram-scale mLIB pouch cells can exceed 30 weight% (wt%) (Digikey, 1568-1496-ND), while a 40-gram LIB has a significantly lower package overhead of approximately 10 wt%[23]. Additionally, the small-scale quadrotor places stringent demands on its onboard power sources, simultaneously requiring miniaturization, high energy density, and high power density[14,24]. However, most commercially available mLIBs are developed for low-power applications and are not optimized for the high power drains of small-scale quadrotors, further contributing to the short flight duration of the mLIB-powered small-scale quadrotor.

In order to extend flight durations and increase the efficiency of small-scale quadrotors, this study explores alternative chemistries for the on-board power system. Metal-air battery chemistry is a promising candidate for extending the flight duration of the small-scale quadrotor due to its exceptionally high theoretical energy density. Generally, metal-air batteries are categorized into two types based on electrolyte materials: aqueous-electrolyte-based metal-air batteries, and organic-solvent-electrolyte-based metal-air batteries. Among these, aqueous-electrolyte-based metal-air batteries are particularly compelling for small-scale quadrotor applications due to their superior power performance[25]. This superior performance originates from the enhanced ionic conductivity and electrode reaction kinetics of the aqueous environment[26]. Figure 1 (B) compares the theoretical energy density of various aqueous-electrolyte-based metal-air battery chemistries with the theoretical energy density of conventional LIB chemistry[27,28]. All aqueous metal-air battery chemistries show a theoretical energy density above 1000 $\frac{Wh}{kg}$, which is significantly higher than the theoretical energy density of 500 $\frac{Wh}{kg}$ for the conventional LIB chemistry. In addition, the aqueous electrolyte chemistry is generally regarded as safer and more environmentally friendly compared to the organic electrolytes typically found in commercial Li-ion batteries[29–31].

Among aqueous-electrolyte-based metal-air batteries, aluminum-air batteries (AABs) can deliver a remarkable theoretical specific energy of 8100 $\frac{Wh}{kg}$, which is an order of magnitude higher than the conventional LIB chemistry. The advantage of AABs is further augmented by the stability of AAB cell components when exposed to the ambient over the operational duration of the small-scale quadrotor, as well as the reliance of the cathode on oxygen from the air for its electrochemical reaction[32]. Therefore, the hermetic packaging that is often required for other battery types to mitigate rapid atmospheric degradation is not necessary for AABs. As a result, AABs can be housed in simpler packages that serve only to contain the electrolyte, markedly reducing the packaging weight. In addition, the AAB also shows a superior power performance to other aqueous-based metal-air batteries, which is partially due to the highest theoretical open circuit voltage (OCV)[33]. Therefore, the AAB chemistry is a promising approach to provide sufficient energy density and power density for the small-scale quadrotor.

However, it should be noted that the aqueous AAB chemistry is typically a primary (non-rechargeable) energy source, which may limit their use in some scenarios[34]. Despite this, small-scale quadrotors are commonly

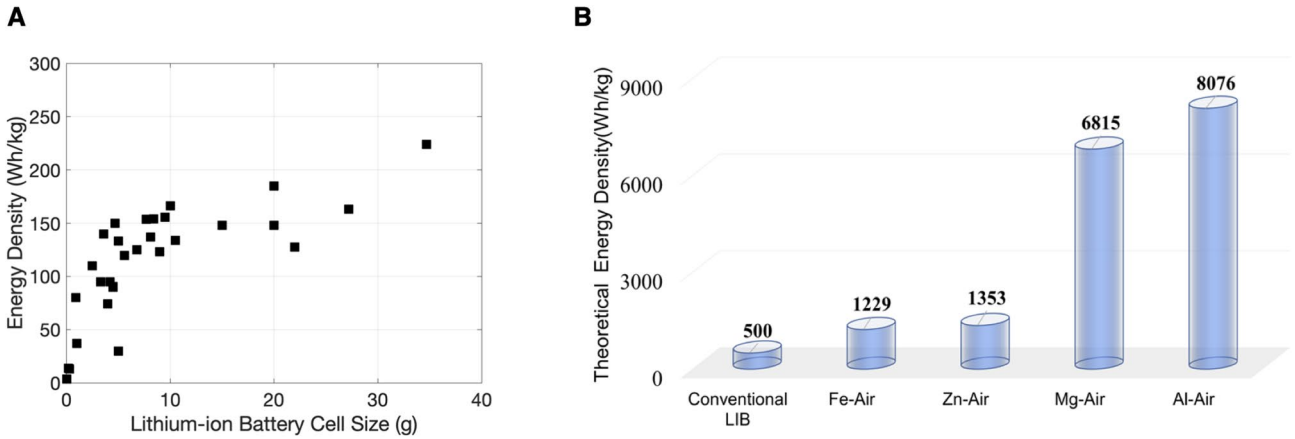

Fig. 1. (**A**) Correlation between LIB cell size and gravimetric energy density. The gravimetric energy density decreases with decreasing LIB weight; **B**) Theoretical energy density comparison between the conventional LIB chemistry and various metal-air battery chemistries.

deployed in mission-critical tasks including search and rescue operations, mining exploration, or environmental monitoring in hazardous or remote locations[35,36]. In such cases, the primary operational requirement is not the rechargeability of the battery but the ability to sustain long-duration flights, as retrieving the small-scale quadrotor to recharge the battery is often impractical or impossible in some cases[37]. For example, in rescue missions or when collecting critical data from remote or hazardous areas, the focus shifts to maximizing flight duration to insure the safety of the data collection personnel.

A typical aqueous-electrolyte-based AAB is comprised of an aluminum (Al) anode, an aqueous alkaline electrolyte, and an air cathode. Figure 2 shows a schematic of the working mechanism of the AAB. The overall electrochemical reaction of the AAB is given in Eq. 7. Under discharge, the Al anode is oxidized to aluminum hydroxide, as shown in Eq. 8. Oxygen diffuses through the cathode and is reduced at the electrolyte-cathode interface, as shown in Eq. 9. The oxygen reduction reaction typically relies on expensive catalysts, such as platinum, to achieve high power density, which can significantly raise the overall cost. However, recent advancements have demonstrated the potential of cost-effective alternative catalysts to meet power requirements at a significantly lower cost[8,38].

Despite all the advantages mentioned above, the aqueous AAB has long been criticized for rapid anode corrosion in its alkaline aqueous electrolyte. In parallel with the oxidation of Al, there is a parasitic reaction involving the reduction of water, resulting in hydrogen gas generation at the surface of Al anode, as shown in Eq. 10. Equation 9 and Eq. 10 are competing reactions on the surface of Al exposed to the alkaline electrolyte. This undesirable parasitic reaction leads to anode consumption without contributing to electron flow in the external circuit, which in turn, reduces the anode utilization. Such rapid corrosion has been a barrier to the adoption of AAB technology in devices where long-term operation is required, such as electronics, electric vehicles, and off-grid power supplies[39]. Interestingly, the typical corrosion issues that limit the use of AABs in intermittent, long duration applications are less of a concern in the small-scale quadrotor application, where the battery is typically under continuous use over a short period of time.

$$4Al + 3O_2 + 6H_2O \rightarrow 4Al(OH)_3 \tag{1}$$

$$Al + 3OH^- \rightarrow Al(OH)_3 + 3e^- \tag{2}$$

$$O_2 + 2H_2O + 4e^- \rightarrow 4OH^- \tag{3}$$

$$2H_2O + 2e^- \rightarrow H_2 + 2OH^- \tag{4}$$

Herein we exploit the potential of the AAB chemistry, namely minimal packaging overhead, high energy density, and high power density, to design gram-scale micro-AABs (mAABs). The mAABs studied here are based on a

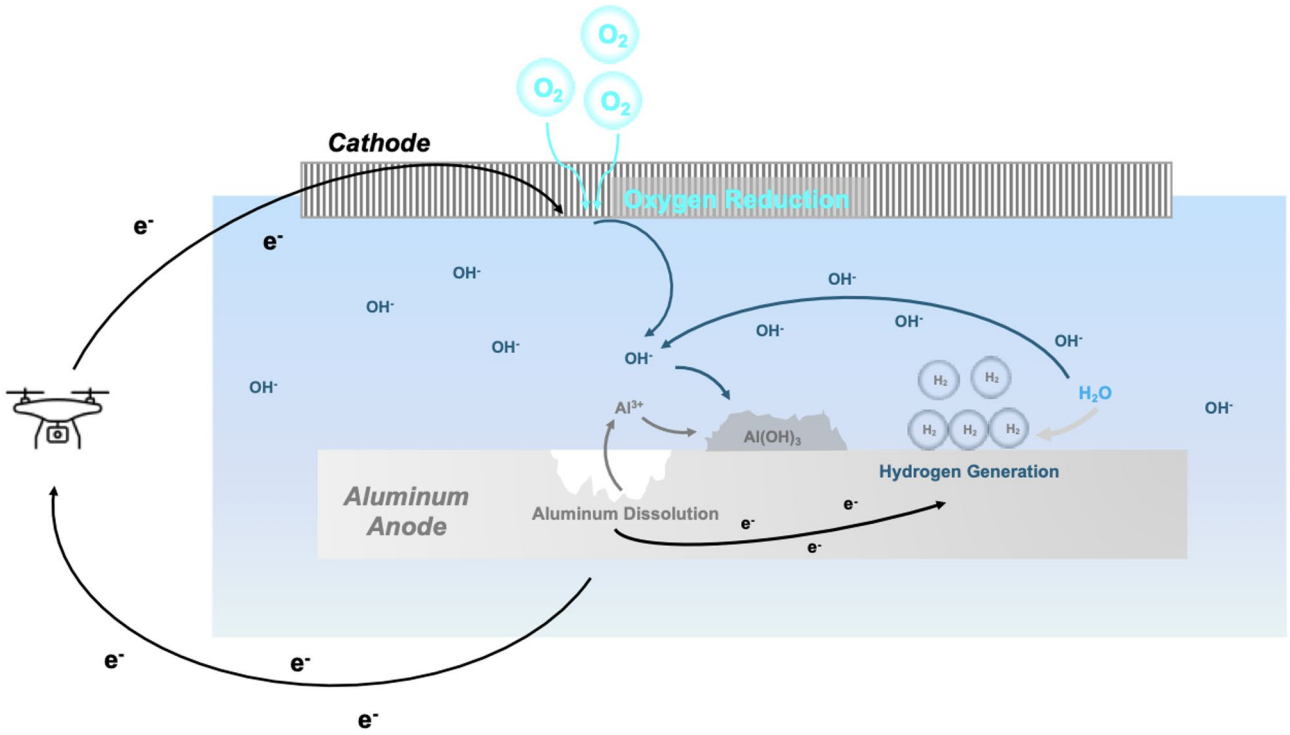

Fig. 2. Schematic of the electrochemical mechanisms taking place in aqueous-electrolyte AABs. In the main reaction, oxygen is reduced at the cathode and Al is oxidized at the anode, forcing current through the external circuit. In the competing corrosion reaction, water is reduced to hydrogen and Al is oxidized without external current flow.

pouch cell design. We present a weight-efficient packaging approach for mAAB fabrication, and engineer both the anode and the electrolyte to achieve the necessary gravimetric power density to ensure small-scale quadrotor liftoff while simultaneously maintaining high gravimetric energy density for extended duration operation. We then integrate the mAAB with a 3D printed small-scale quadrotor and characterize its performance to evaluate the practicality of the mAAB as an onboard power source, and compare the obtained results from a mLIB integrated on the same platform.

Results and discussion

Micro aluminum-air battery cell fabrication with lightweight package

To maximize the gravimetric energy and power density at the AAB cell level, it is imperative to minimize battery packaging that adds weight without contributing to electrochemical performance. For aqueous electrolyte AABs, the primary function of the battery package is to properly contain the electrolyte within the cell. Typically, the cathode of an AAB is constructed using a carbon cloth, impregnated with a layer of Polytetrafluoroethylene (PTFE). This hydrophobic carbon cloth cathode effectively retains the aqueous electrolyte. Supplementary Material Figure S1 shows an image of aqueous electrolyte beading on the hydrophobic PTFE-treated carbon cloth cathode. Figure 3 (A) shows a schematic exploded view of the proposed mAAB pouch cell, while Fig. 3 (B) shows a photograph of a 2-gram mAAB fabricated in this work next to a US quarter coin for size comparison[6,40,41]. The detailed fabrication process for the mAAB pouch cell can be found in Supplementary Material Figure S2. Briefly, the AAB consists of a 3D-printed polypropylene (PP) frame which acts as a support for both metal-catalyst-bearing hydrophobic carbon cloth cathodes, as well as multiple layers of Al foil anodes. Each Al layer is 1 cm^2 in footprint area. Two punched holes, each 1 mm in diameter, are formed in the Al anodes to facilitate OH^- transport within the multilayer anode structure.

The 3D-printed PP body frame was selected based on key factors such as mechanical integrity, lightweight construction, and thermal and chemical stability. 3D printing minimized material usage while maintaining robust electrode support. Since the frame does not contribute to electrochemical performance, reducing its weight enhances the battery's gravimetric efficiency. PP, with its low density (~0.9 $\frac{g}{cm^3}$), effectively reduces the overall weight without compromising strength. Despite electrolyte temperatures exceeding 80 °C during discharge (as shown in Figure S5, Supplementary Material), PP retains its mechanical integrity, ensuring stability throughout operation. Additionally, PP exhibits excellent chemical stability in the alkaline electrolyte environment, preventing degradation and further ensuring the battery's structural integrity. Experimental tests confirmed the stability and performance of the 3D-printed PP frame during discharge, highlighting its suitability as a lightweight and durable component in this Al-air battery system.

Figure 3 (C) shows the weight breakdown of the 2-gram mAAB pouch cell. Note that the electrochemically inactive packaging materials, including the 3D-printed PP body frame and epoxy for cell assembly, contribute to less than 10 wt% of the total cell weight, compared to the 30 wt% packaging overhead of a gram-scale mLIB. This significant reduction in packaging overhead for the mAAB results from two key factors. First, AAB chemistry does not require hermetic packaging since it is stable in ambient environments over the operational duration of small-scale quadrotors. Second, the carbon cloth serves dual functions as both the battery cathode and the main part of the battery cell packaging, minimizing the amount of packaging material needed.

Aluminum anode optimization

Although the AAB chemistry shows promising theoretical energy density, the practical energy density and power performance of the mAAB must be engineered to support small-scale quadrotor operation. Herein we explore the effect of the Al anode structure on both the power and the energy performance of the mAAB. A commonly used 6M KOH + 100mM sodium stannate (Na_2SnO_3) aqueous electrolyte is utilized here, where the stannate serves as a corrosion inhibitor[42]. Sodium stannate acts as a corrosion inhibitor by preferentially

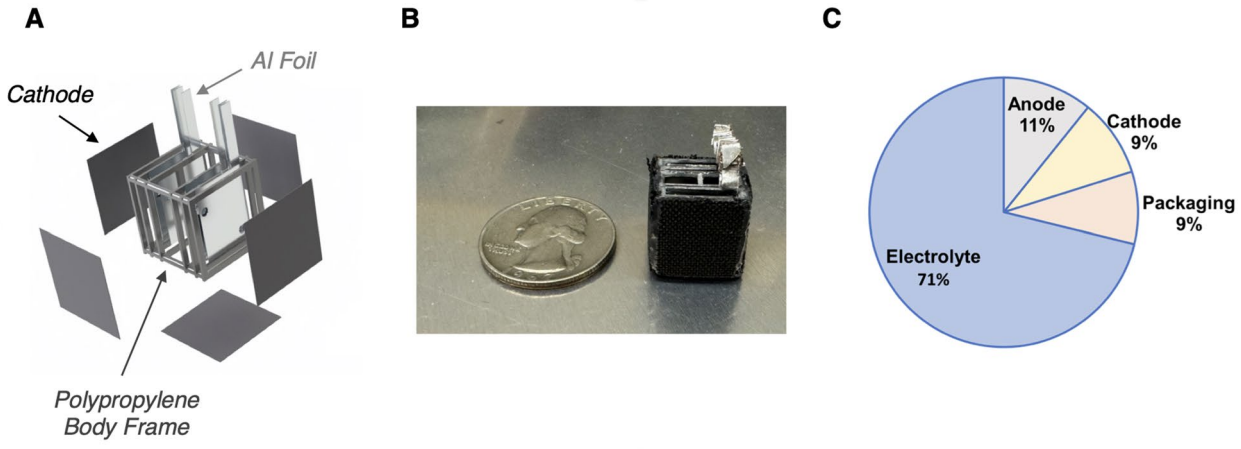

Fig. 3. (**A**) Exploded view of the mAAB; **B**) A photograph of a mAAB pouch cell next to a US quarter coin; C) Weight distribution of the fabricated 2-gram mAAB.

depositing on the cathodic sites of the corrosion reaction on the aluminum surface, thereby reducing the rate of corrosion through the suppression of corrosion kinetics. To examine the effect of the Al anode structure on the power performance, the number of Al anode layers is increased while keeping the cathode area constant. The multilayer anode structure is supported by a multi-layer 3D printed PP cell frame, as shown in Fig. 3 (A). mAAB pouch cells with anodes comprising 1-layer, 2-layers, 4-layers, 6-layers, and 8-layers, in which each layer has a nominal footprint area of 1cm^2, are fabricated. Thus, a one-layer AAB has an anode footprint area of 1 cm^2. However, note that if both sides of an anode layer are exposed to electrolyte, the electrochemically interacting area of the anode will be double that of the footprint area. Footprint area is used as the anode area convention in this work.

The power performance of AABs with different anode structures is compared in Fig. 4 (A). For discharge currents below 0.75 A, the output power density curves for different anode structures tend to cluster together. In contrast, as the current exceeds 0.75 A, the power density curves diverge. The gravimetric power density of cells with different anode structures under a discharge current of 2.1 A is plotted in Fig. 4 (B). Power density increases with the anode electrode footprint area until it reaches 4 cm^2 in footprint area, or 4-layers, at which point the dependence of power density with number of anode layers maintains a relatively constant value at approximately 1000 $\frac{W}{kg_{battery}}$, even with subsequent increases in anode area. This observation illustrates the importance of anode structure on mAAB power performance at the high current levels demanded for quadrotor operation.

To assess the suitability of the mAAB for powering a small-scale quadrotor, the power requirement for operating a commercial small-scale quadrotor, Holystone HS190, is analyzed. This analysis is detailed in the Supplementary Material. The analysis suggests that a discharge power density of 800 $\frac{W}{kg_{battery}}$ at a 2 A discharge can meet the operational demands of this commercial small-scale quadrotor. Figure 4 (B) shows that the mAAB with 4 or more anode layers can achieve this power density requirement.

The conventional view of power performance of a typical air battery is that the cathode is the limiting factor due to the intrinsically sluggish oxygen reduction kinetics[43,44]. However, Fig. 4 reveals a different perspective: at high current levels (e.g., the 2 A utilized here), the power performance also depends on the anode structure. Considering that a single layer of an Al foil anode has a footprint area of 1 cm², when the mAAB pouch cell undergoes a 2 A discharge, the anode current densities based on footprint for 1-layer, 2-layer, 4-layer, 6-layer, and 8-layer mAAB pouch cells are 2 A/cm², 1 A/cm², 0.5 A/cm², 0.33 A/cm², and 0.25 A/cm², respectively. (Recall the anode areal current density used in this work is calculated based on the footprint area of the Al anode foil, which represents half of the electrochemically active surface area of the Al anode foil.) It is likely that these different current densities will result in different overpotentials or other factors in this high-power operational regime.

Anode overpotentials for various anode configurations are measured using a three-electrode system and an anode footprint area of 0.25 cm^2. For each overpotential test, a fresh anode is used, and the discharge current is adjusted to be equal to the corresponding current density for one of the multilayer AABs discussed above. After equilibrating the Al anode with 6M KOH + 100mM Na_2SnO_3 electrolyte for 5 min, the Al anode achieves a stable open circuit voltage (OCV) of −1.87 V vs. a Hg/HgO reference electrode. When a discharge current is applied, the voltage of the Al anode shifts to a more positive value due to the effect of overpotential. Figure 5 (A) shows the measured Al anode voltage for different equivalent number of anode layers. The overpotential is defined as the difference between OCV and the discharge voltage, which is calculated for each anode structure and summarized in Fig. 5 (B).

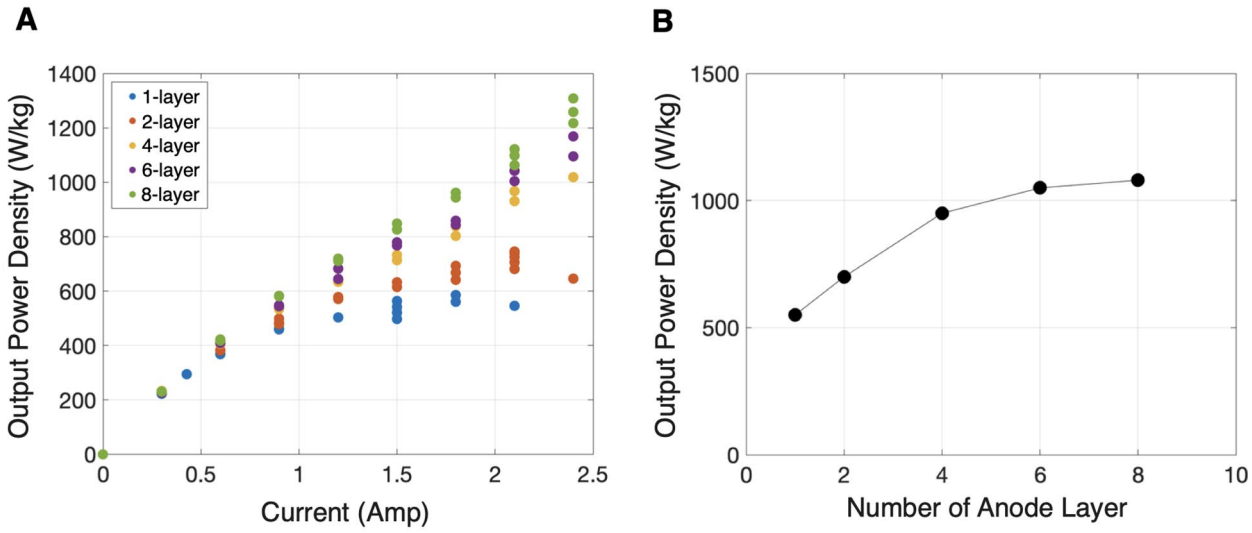

Fig. 4. (**A**) Power performance of mAAB pouch cells with different anode structures; **B**) Power density of mAAB pouch cells with different anode structures at 2.1 A.

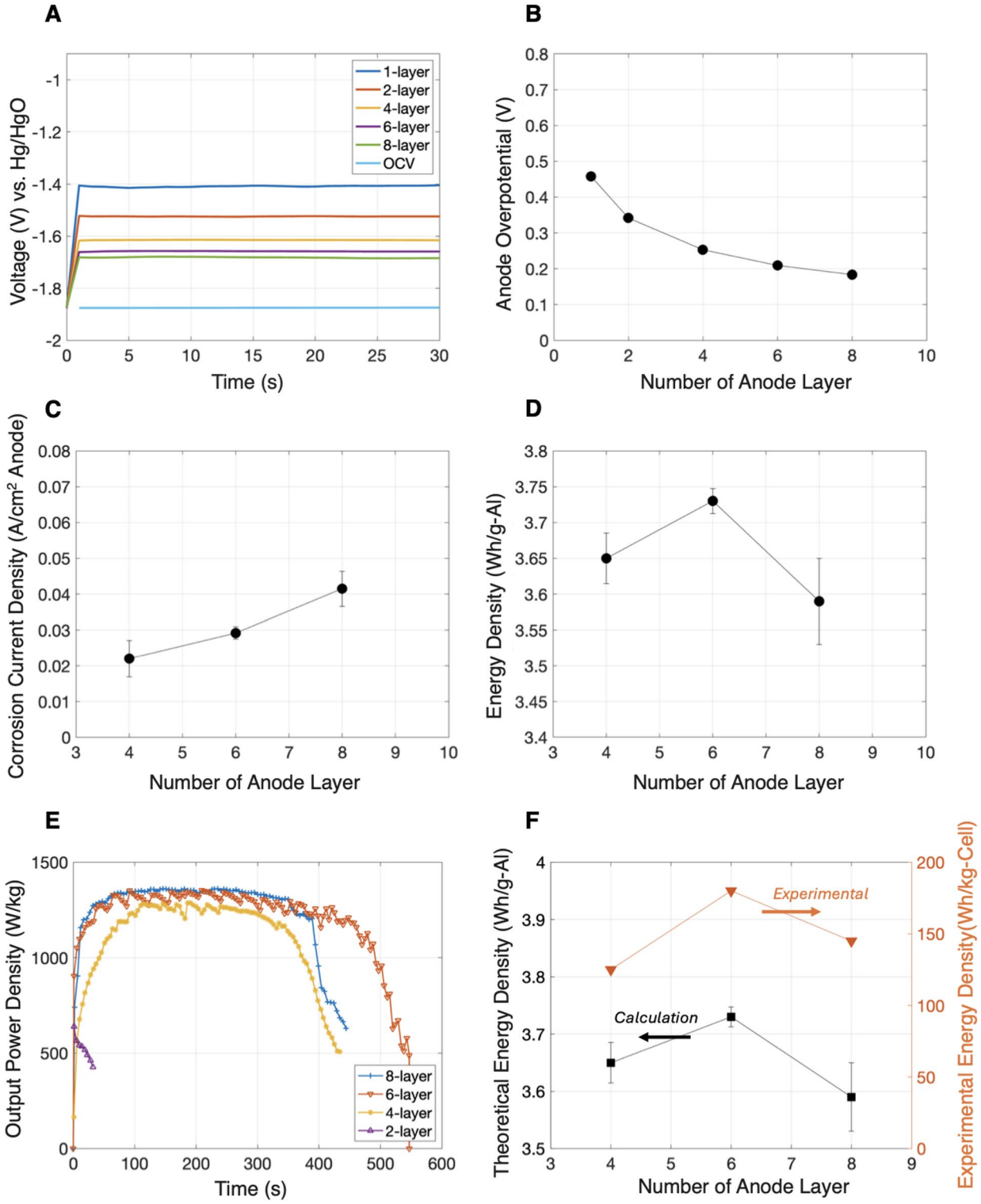

Fig. 5. (**A**) and (**B**) Al anode voltage measured in a three-electrode system for different anode structures; **C**) Corrosion current density determined from anode mass loss measurements for different anode structures; **D**) Calculated energy performance for different anode structures; **E**) 2 A constant current discharge from mAAB pouch cells with anode structure of 2-layer, 4-layer, 6-layer and 8-layer; **F**) The measured discharge energy density above the 800 $\frac{\mathrm{W}}{\mathrm{kg}_{\mathrm{battery}}}$ power threshold compared with the calculated mAAB energy density. Note that the former is on a per-cell basis, while the latter is on a per-anode-mass basis; however, the functional forms are similar and lead to the same optimal number of anode layers.

The overpotential of the Al anode monotonically decreases as the number of anode layers increases; however, the rate of this decrease begins to level off with the addition of more layers. This trend suggests the significant impact of anode structure on the anode overpotential of the mAAB. The overall anode area increases with the number of Al anodes, resulting in a lower anode current density and consequently reducing the anode overpotential. As the number of anode layers increases, the reductions in overpotential become less marked, suggesting that the optimization of power performance through anode structural engineering is nearing its practical limits.

Although increasing the anode area is beneficial for enhancing power performance, it can decrease energy performance due to corrosion. To investigate this effect, corrosion current densities for various anode configurations are measured using the three-electrode system. For each corrosion current test, a fresh anode is used, and the discharge current is adjusted to be equal to the corresponding current density for one of the multilayer AABs calculated above. We assume there are two dominant pathways for mass loss during the discharge of the mAAB: coulombic consumption of the Al anode from the discharge, and corrosion consumption of the Al anode. Under this assumption, the corrosion current, I_{corr}, can be calculated as follows:

$$I_{corr} = \frac{(m_{final} - m_{initial} - m_{coulumbic}) \times Time}{3000 \frac{mAh}{g\ Al}}$$

where m_{final} and $m_{initial}$ are the experimental masses of the Al anode before and after the corrosion testing, respectively, and $m_{coulumbic}$ represents the mass loss of the Al anode attributable to the discharge current, which is calculated from the experimental current, time, and theoretical capacity of Al ($3000 \frac{mAh}{g\ Al}$). Figure 5 (C) shows the corrosion current density determined from mass and current-time measurements for 4-layer, 6-layer, and 8-layer anode structures. The measurement for each anode structure is repeated two times to calculate the standard deviation error bar. It is observed that the corrosion current density increases with the number of anode layers. This trend can be attributed to the reduced overpotential in anodes with more layers, which consequently increases the driving force for the corrosion reaction. In addition, the anode structure with more layers leads to a larger Al electrode area, further amplifying the Al anode mass loss due to corrosion.

The discussion highlights a critical tradeoff in the anode structure design: while a higher anode area can increase the discharge voltage, it may simultaneously reduce the discharge capacity. Since the discharge energy is the product of the discharge voltage and the discharge capacity, the tradeoff of the anode structure might lead to an anode structure with optimal energy performance in this design space. Therefore, an optimal anode structure can be predicted from a calculated energy density using Eq. 5 to Eq. 7, where η is the overpotential:

$$V_{Cell} = OCV - \eta_{Anode} - \eta_{Cathode} - \eta_{Electrolyte} \tag{5}$$

$$Discharge\ Capacity = Capacity_{thoeretical} \times \frac{I_{Discharge}}{I_{Discharge} + I_{Corrosion}} \tag{6}$$

$$Discharge\ Energy = V_{Cell} \times Discharge\ Capacity \tag{7}$$

Assuming $\mathrm{OCV} - \eta_{\mathrm{Cathode}} - \eta_{\mathrm{Electrolyte}} = 1.5\mathrm{V}$ and $\mathrm{I_{Discharge}} = 2\mathrm{A}$, the discharge energy density is calculated. As shown in Fig. 5 (D), calculations suggest that the optimal energy density performance is achieved with a 6-layer anode structure.

To test this optimization, the experimental discharge performance of mAAB pouch cells with varying numbers of Al anode layers is evaluated. Figure 5 (E) shows the 2 A constant current discharge for pouch cells with anode structure of 2-layer, 4-layer, 6-layer, and 8-layer. The specific Al anode configurations for different anode structures are as follows:

- 2-layer: two 500 μm thick Al foils.
- 4-layer: four 200 μm thick Al foils.
- 6-layer: two 200 μm Al foils and four 100 μm Al foils, with the four 100 μm Al foils positioned between the two 200 μm Al foils.
- 8-layer: eight 100 μm thick Al foils.

Note that the mAAB cells with anode structures of 4-layer, 6-layer, and 8-layer maintain a constant total Al anode mass.

The 2-layer cell has the lowest discharge power density, beginning at 600 $\frac{W}{kg_{battery}}$, but decaying rapidly within the initial 50 s of the discharge. As a comparison, cells with 4-layer, 6-layer, and 8-layer anode structures can sustain the 2 A discharge, with each demonstrating a discharge power density plateau well above the 800 $\frac{W}{kg_{battery}}$ threshold under the 2 A discharge. The plateau power density increases slightly as the number of anode layers increases. Figure 5 (F) compares the measured discharge energy density (terminating when the power density falls below the 800 $\frac{W}{kg_{battery}}$ threshold) with the calculated discharge energy density for 4-layer, 6-layer, and 8-layer cells.

The discharge performance shown in Fig. 5 (E) agrees with the power performance data shown in Fig. 4 (A), confirming that the 2-layer anode structure is not able to sustain a 2 A discharge above 800 $\frac{W}{kg_{battery}}$; and also that power performance increases with more anode layers. However, despite the 8-layer cell achieving the highest discharge power density plateau, it does not translate to the highest discharge energy density. Instead,

the 6-layer cell shows the highest energy density and the longest discharge duration. This trend aligns with the calculated result regarding corrosion optimization. This study suggests that when the mAAB is used in high-power applications (e.g., small-scale quadrotors), the anode/cathode footprint ratio (A/C ratio) can significantly affect both energy and power performance. For this mAAB pouch cell design, when the discharge current is 2 A, an A/C ratio of 1.1, corresponding to the 6-layer anode structure, leads to improved discharge performance due to a balance of the Al anode overpotential and the corrosion at the Al anode. Moving forward, the 6-layer anode structure will be utilized for future steps in this work.

Electrolyte optimization

In this section, the impact of electrolytes on the electrochemical performance of mAABs is studied. The electrolyte serves as the medium for Al anode oxidation, Al anode corrosion, cathode oxygen reduction, and OH^- ion transport, all of which have a significant impact on the energy and power performance of the mAAB. In theory, a smaller quantity of electrolyte is preferable for enhanced gravimetric performance; however, due to electrolyte degradation over discharge, especially under high-rate discharge, there is a minimum requirement on electrolyte quantity[45].

Figure 6 (A) compares power performance between cells using fresh electrolytes, freshly prepared just before testing, and used electrolytes, taken after the discharge power density falling below 800 $\frac{W}{kg_{battery}}$ under the 2 A discharge. A cell containing used electrolyte and fresh Al anode shows a marked decline in power performance compared to a cell with fresh electrolyte and fresh Al anode. Specifically, the cell with the used electrolyte has fallen from a peak power exceeding 1000 $\frac{W}{kg_{battery}}$ to 500 $\frac{W}{kg_{battery}}$. To understand the origin of the power performance decay, a OH^- ion titration protocol is developed (see Supplementary Material). The titration results show that the used electrolyte has a KOH concentration of only 3 M, a substantial drop from the 6M KOH at the beginning of the discharge. To discern the impact of OH^- ion depletion on the power performance and to separate its impact from other potential factors such as water consumption in the electrolyte or the buildup of side products in the electrolyte, a rejuvenated electrolyte experiment is conducted. KOH solid pellets are introduced to the used electrolyte to rejuvenate its KOH concentration to 6 M, and this rejuvenated electrolyte is used together with fresh Al anode. Figure 6 (A) compares the power performance of the cell with fresh 6M KOH, the cell with used 3M KOH, and the cell with rejuvenated 6M KOH. The power comparison shows that the power performance of the cell with rejuvenated 6M KOH is significantly improved compared to that of the used 3M KOH and aligns closely with that of the fresh 6M KOH cell.

Figure 6 (A) suggests that the availability of the OH^- ion in the electrolyte can significantly impact the power performance of the mAAB. When the OH^- ion concentration drops from 6 M to 3 M, the kinetics of the mAAB can no longer support the 2 A discharge, thus halting the discharge. The OH^- ion concentration in the electrolyte can affect the power performance in at least two ways. First, for AABs operating with alkaline electrolytes, cathode reaction kinetics are generally enhanced at higher OH^- ion concentrations. Second, there is an optimal ionic conductivity observed at a 6M KOH concentration[46]. Both these phenomena are negatively affected as the pH of the electrolyte falls due to OH^- consumption.

There are two main pathways through which OH^- ions are consumed. First, as the electrolyte is exposed to air, OH^- ions can react with carbon dioxide, leading to carbonation, as illustrated in Eq. 8. Second, Eq. 9 and Eq. 10 show the slow recovery of OH^- ions from the decomposition of aluminate, $Al(OH)_4^-$. During the discharge, aluminate ions, serving as intermediate species, are generated at the Al anode. This generation process results in the consumption of OH^- ions, which should ideally be regenerated when aluminate ions break down into aluminum hydroxide. However, under conditions of high current discharge, it is likely that the rate of aluminate decomposition is much slower than its generation rate, resulting in a net decrease in OH^- ion concentration in the electrolyte. Given that the discharge duration of the mAAB is limited to approximately 10 min, the impact of the electrolyte carbonation on OH^- depletion is considered to be minor, and the slow recovery from $Al(OH)_4^-$ is considered as the dominant consumption mechanism for the high-discharge-rate mAAB. Based on these insights, two strategies are proposed to prolong the discharge duration: increasing the OH^- ion concentration in the electrolyte and adjusting the mass ratios between the electrolyte and the anode. The subsequent discussion investigates the optimal electrolyte composition, followed by the identification of an optimal mass ratio between the electrolyte and the anode.

$$CO_2 + 2OH^- \rightarrow CO_3^2 + H_2O \tag{8}$$

$$Al + 4OH^- \rightarrow Al(OH)_4^- + 3e^- \tag{9}$$

$$Al(OH)_4^- \rightarrow Al(OH)_3 + OH^- \tag{10}$$

Figure 6 (B) shows the 2 A constant current discharge curve across various electrolyte compositions, ranging from 4 M to 8M KOH, all with 100 mM Na_2SnO_3. Figure 6 (C) summarizes the energy density for cells with various electrolyte compositions when above the power threshold, 800 $\frac{W}{kg_{battery}}$. Among these, the 7M KOH + 100 mM Na_2SnO_3 electrolyte exhibits the highest energy density, achieving 230 $\frac{Wh}{kg_{battery}}$ when above the power density threshold, a 30% improvement over the commonly used 6M KOH + 100 mM Na_2SnO_3 electrolyte.

The trend observed from 4 M to 7 M shows that discharge energy density increases with higher concentrations of OH^- ion, supporting the theory that the availability of the OH^- ion is critical for extending discharge duration under the 2 A discharge. However, a decline in energy density occurs as the concentration increases

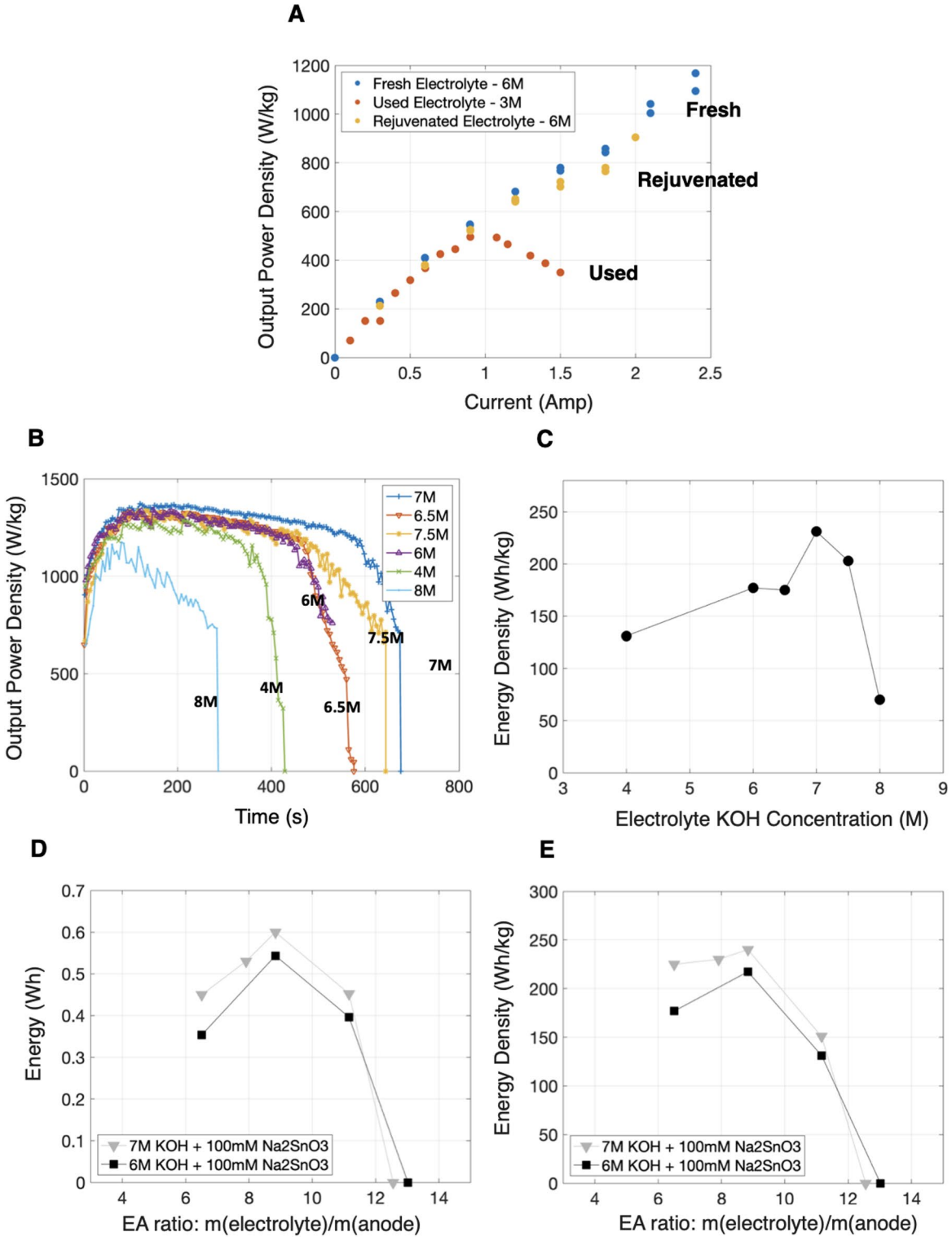

Fig. 6. (**A**) Power performance comparison between mAAB cells using fresh electrolytes, used electrolytes and rejuvenated electrolytes; **B**) 2 A discharge curves for cells across various electrolyte compositions, ranging from 4 M to 8M KOH, all with 100 mM Na_2SnO_3; **C**) Summarized discharge energy density of cells with different electrolyte compositions when the power density is above the power threshold value – 800 $\frac{W}{kg_{battery}}$; **D**) Discharge energy output of cells, under a 2 A discharge when above 800 $\frac{W}{kg_{battery}}$, with different EA ratios for both the 7M KOH + 100 mM Na_2SnO_3 electrolyte and the 6M KOH + 100 mM Na_2SnO_3 electrolyte; **E**) Discharge energy density output of cells under a 2 A discharge when above 800 $\frac{W}{kg_{battery}}$ with different EA ratios for both the 7M KOH + 100 mM Na_2SnO_3 electrolyte and the 6M KOH + 100 mM Na_2SnO_3 electrolyte.

beyond 7 M to 8 M. Although increasing the concentration of OH^- ion from 7 M to 8 M has been shown to have slightly reduced electrolyte ionic conductivity, this level of decrease is likely insufficient to explain the significant decrease in power performance[46]. Instead, the observed decline in energy density may be attributed to accelerated Al anode corrosion at higher KOH molarities. Moreover, the Al anode corrosion is an exothermic reaction, leading to temperature increases that can further increase the corrosion rate. When the rate of the corrosion reaches or exceeds an apparent threshold, as seen in the 8M KOH + 100 mM Na_2SnO_3 electrolyte, the cell initiates a self-heating mechanism, which can in turn further accelerate the corrosion rate, potentially placing the cell in a corrosion-limited operational regime. This corrosion limitation theory is supported by measurements of the cell electrolyte temperature and the OH^- concentration of the electrolyte at the end of discharge (see Supplemental Material). Thus, the electrolyte composition of 7M KOH + 100 mM Na_2SnO_3 is identified as the optimal electrolyte composition for the mAAB under a 2 A discharge.

As discussed previously, due to the OH^- consumption during discharge, increasing the amount of OH^- ion in the electrolyte is promising for enhanced electrochemical performance. However, despite an increased amount of OH^- ion, raising the KOH concentration beyond 7 M will not necessarily lead to enhanced electrochemical performance due to the corrosion. Therefore, increasing the amount of OH^- ions through loading more electrolyte is investigated. Figure 6 (D) shows the discharge energy of cells under a 2 A discharge when above 800 $\frac{W}{kg_{battery}}$ with different mass ratios between the anode and the electrolyte (EA ratio) for both the 7M KOH + 100 mM Na_2SnO_3 electrolyte and the 6M KOH + 100 mM Na_2SnO_3 electrolyte. To adjust the EA ratio, the mass of the electrolyte is varied while maintaining a constant Al anode mass. The cells with the 7M KOH + 100 mM Na_2SnO_3 electrolyte consistently demonstrate higher discharge energy across all investigated EA ratios compared to the 6M KOH + 100 mM Na_2SnO_3. Figure 6 (E) shows the energy density under the 2 A discharge above 800 $\frac{W}{kg_{battery}}$, that both electrolyte compositions demonstrate a peak energy density at an EA ratio of 8.8. However, the energy density for both electrolytes drops to zero when the EA ratio increases beyond 12. Note that an energy density of zero on this graph does not mean no cell output; instead, it means that the cell could not achieve a power density exceeding 800 $\frac{W}{kg_{battery}}$.

The enhanced energy performance of the 7M KOH + 100 mM Na_2SnO_3 electrolyte compared to the 6M KOH + 100 mM Na_2SnO_3 is consistent with earlier discussions regarding optimal electrolyte composition. For the 7M KOH + 100 mM Na_2SnO_3 electrolyte curve in Fig. 6 (E), the maximum energy density suggests that the EA ratio of 8.8 results in a good balance of electrolyte performance and Al anode performance. Furthermore, the anode utilization rate, which is a critical indicator of the Al anode's efficiency and is calculated from dividing discharge capacity by the total available capacity of the Al anode, reaches over 70% for the mAAB. Therefore, the EA ratio of 8.8 is identified as optimal. Further increases in the EA ratio beyond the optimal lead to a decline in energy density, resulting from inefficient electrolyte usage due to disproportionate EA ratios. When the EA ratio further increases above 12, the excess electrolyte significantly reduces the gravimetric performance, resulting in the mAAB being unable to discharge above 800 $\frac{W}{kg_{battery}}$. While the corrosion challenges associated with Al-air batteries have historically limited their application, this experimental result, showing over 70% utilization of the aluminum anode during flight, indicate that the engineered cell design can mitigate the corrosion issue in this specific application. However, it should be noted that the current cell design may not be fully optimized, and a comprehensive simulation study on the cell design could potentially further enhance its performance. In addition, although the present system achieves anode utilization above 70%, further improvements in anode utilization are possible. Strategies such as employing aluminum alloys, incorporating corrosion inhibitors, or exploring organic electrolytes could reduce corrosion and enhance anode-use efficiency, thereby extending the discharge duration of the battery.

Figure 7 (A) presents a Ragone plot comparing the energy and power performance between the mAAB and the mLIB. Two commercially available mLIB cells of different sizes, 6.8 g and 2.8 g, which are used in powering commercial small-scale quadrotors (HolyStone HS190 and Cheerson CX10), are examined. Figure 7 (A) shows that the larger 6.8-gram mLIB cell outperforms the smaller one, likely due to reduced packaging overhead. The package overhead for the LIB is often less significant in larger cells. In contrast, the smaller 2.5-gram mAAB cell, using 7M KOH + 100 mM Na_2SnO_3 electrolyte with an EA ratio of 8.8, exhibits significantly superior performance. Under a discharge power density of 800 $\frac{W}{kg_{battery}}$, the 2.5-gram mAAB cell demonstrates an energy density of 240 $\frac{Wh}{kg_{battery}}$, which is a threefold improvement in energy density over the 2.8-gram mLIB cell. Furthermore, it is reported that 500 $\frac{W}{kg_{battery}}$ is sufficient for powering more power-efficient small-scale quadrotors[14]. When the power density requirement is lowered to 500 $\frac{W}{kg_{battery}}$, the energy density of the mAAB increases further. A 2-gram mAAB cell delivers an energy density of 325 $\frac{Wh}{kg_{battery}}$ when above 500 $\frac{W}{kg_{battery}}$. This represents a substantial 4.3-fold increase in energy density compared to the 2.8-gram mLIB cell. Additionally, Fig. 7 (B) presents a Ragone plot comparing the energy and power performance of the mAAB from this work with those reported in the literature[47–51]. The comparison shows that the mAAB from this work simultaneously achieves both high energy density and high power density, outperforming previous AABs.

Micro aluminum-air battery performance assessment using a commercial small-scale quadrotor

The practical flight duration of the mAAB is assessed using a commercial small-scale quadrotor, Holy Stone HS190. The HS190 small-scale quadrotor weighs 23 g, including a 6.8-gram mLIB cell. Utilizing 3D printing

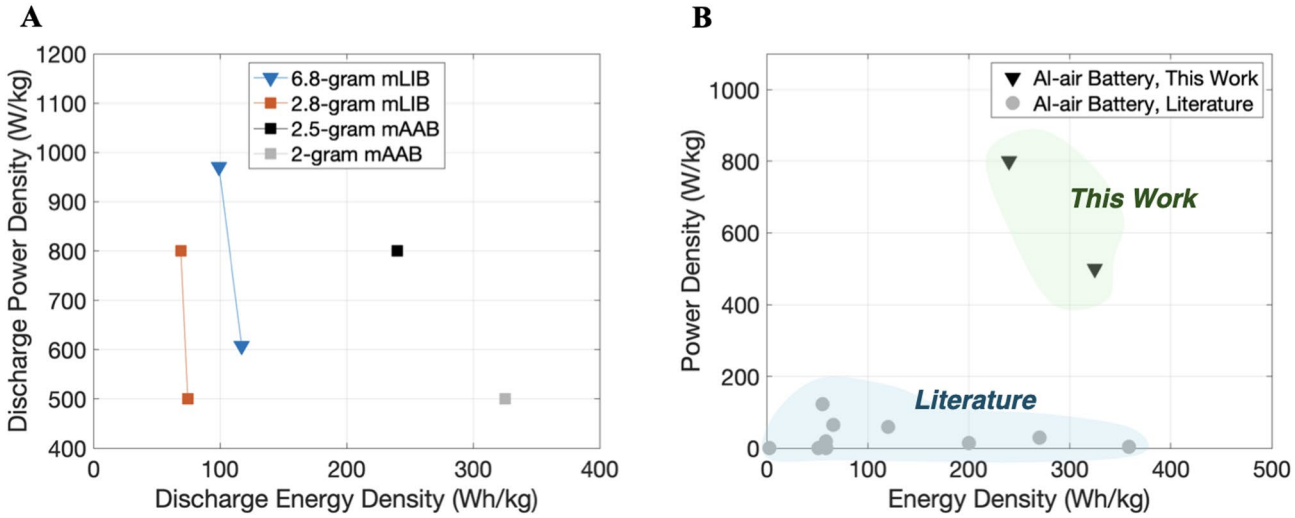

Fig. 7. (**A**) Ragone plot comparing the mLIB and the mAAB; **B**) Ragone plot comparing mAABs from this work with mAABs reported in literature.

technology, a customized quadrotor body is created, allowing facile integration of the HS190 operational components and the mAAB. Four mAAB cells are connected in series to meet the voltage requirement of the HS190. The off-the-shelf HS190 propulsion system and control circuitry are transplanted to the 3D-printed body frame. The term body frame refers to the only the body frame of the micro-quadrotor, not including battery, motors, propellers and wiring. Subsequent tests confirm that the 3D-printed small-scale quadrotor platform can maintain a stable flight. Figure 8 (A) shows a photo of the integrated platform with the HS190 onboard control system and propulsion system, together with the mAAB pack. The integration of Al-air batteries with micro-quadrotors imposes some challenges as the Al-air battery has a larger volume compared to lithium-ion batteries of equivalent mass. However, through optimized design and component arrangement, the Al-air battery pack is successfully into the quadrotor frame without significantly impacting its balance or performance. The weight distribution of components was similar to that of other micro-quadrotor platforms powered by lithium-ion batteries, as shown in Fig. 8 (B)[14].

The flight duration of the small-scale quadrotor is evaluated using two versions of the mAAB pack: an 8-gram mAAB pack and a 10-gram mAAB pack. The 8-gram mAAB pack comprises four 2-gram AAB connected in series, each with an EA ratio of 6.5. The 10-gram mAAB pack consists of four 2.5-gram mAABs connected in series, each with an EA ratio of 8.8. Figure 8 (C) shows a successful flight of the small-scale quadrotor powered by the mAAB. When equipped with the 8-gram mAAB pack, the small-scale quadrotor achieves a flight duration of 8.75 min. The small-scale quadrotor powered by the 10-gram mAAB pack further extends this duration to 13.1 min. Both mAAB pack configurations significantly surpass the flight duration of 4.5 min provided by the small-scale quadrotor powered by the off-the-shelf 6.8-gram mLIB. Figure 8 (D) plots the discharge duration under a 2 A discharge when above 800 $\frac{W}{kg_{battery}}$ and the flight duration for both the mAAB and the mLIB. Under both testing conditions, the mAAB shows consistently improved performance compared to the mLIB. This finding suggests that the Al-air battery system achieves a comparable level of overall efficiency, particularly when applied to small-scale quadrotor operations.

Despite using the same customized small-scale quadrotor platform in all flight duration tests, the variations in the battery size pose challenges in accurately quantifying the flight duration improvement attributable to the superior performance of the mAAB. To isolate the mAAB's improvements from the impact of the battery size, hypothetical flight durations for 8-gram and 10-gram mLIB cells are calculated, under the assumption that mLIB gravimetric electrochemical performance does not change with a slightly increased size. In this calculation, it is assumed that both the battery energy density ($E\frac{\mathrm{Wh}}{kg_{battery}}$) and the platform-level power density ($P\ \frac{W}{kg_{takeoff}}$) remain constant. The relationship between the mass ratio ($r = \frac{m_{battery}}{m_{takeoff}}$) and the flight duration (t) is described by Eq. 11, which shows that the flight duration linearly increases with the mass ratio (r) when both the battery energy density and platform-level power density are held constant.

$$t = \frac{E}{P}\frac{m_{battery}}{m_{takeoff}} \tag{11}$$

Based on the actual flight duration measured using the 6.8-gram mLIB, hypothetical flight durations for 8-gram and 10-gram mLIB configurations are calculated to be 5.05 min and 5.9 min, respectively. In contrast, the measured flight durations for the 8-gram and 10-gram mAAB packs are 8.75 min and 13.1 min, respectively, reflecting improvements of 73% and 122% over their mLIB counterparts of comparable size. These findings not

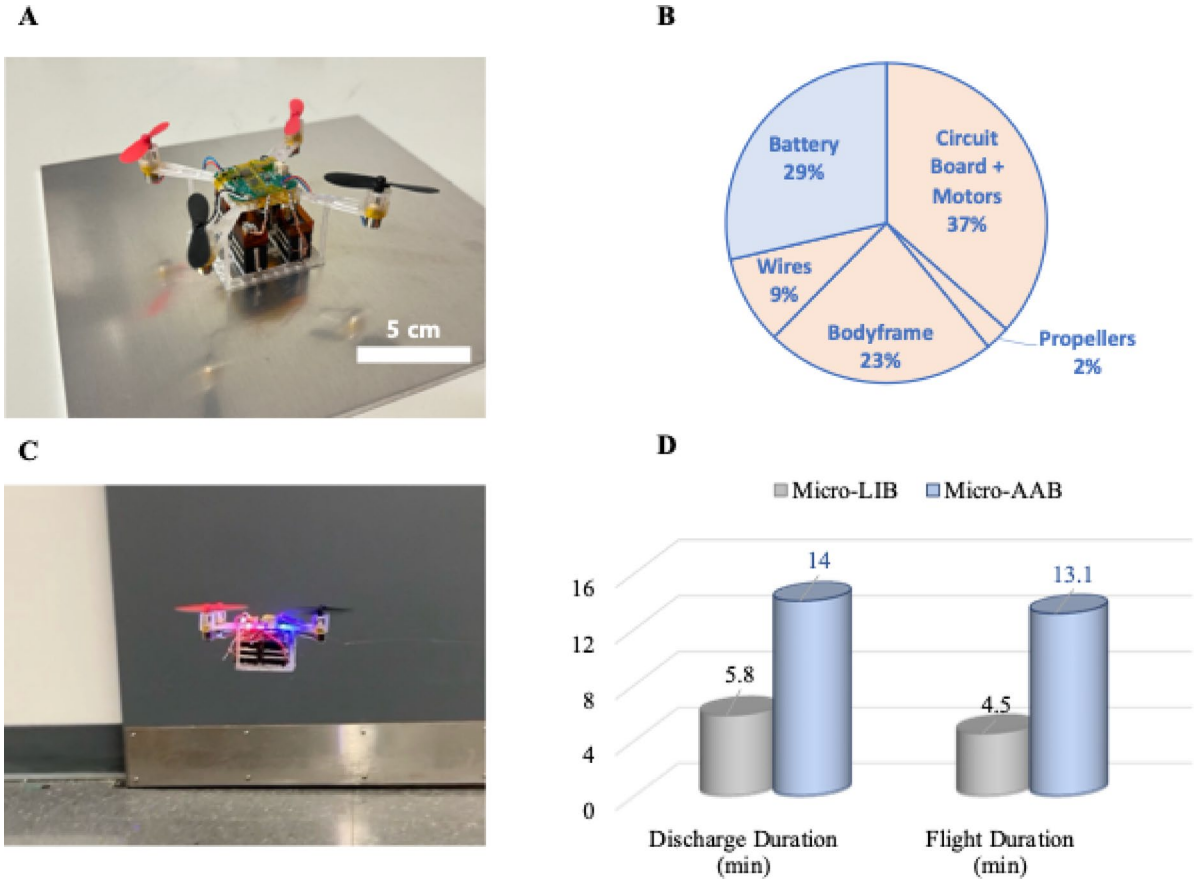

Fig. 8. (**A**) A photo of the customized small-scale quadrotor powered by the mAAB pack; **B**) Weight distribution of the customized small-scale quadrotor powered by an 8-gram mAAB pack; **C**) A mAAB-powered small-scale quadrotor in untethered flight; **D**) Discharge duration and flight duration comparisons between the mLIB and the mAAB.

only demonstrate the enhanced flight duration offered by the mAAB but also mark the first successful attempt at powering a small-scale quadrotor in untethered flight conditions using mAABs.

Conclusion

AAB chemistry is identified as a promising chemistry for extending the flight duration of small-scale quadrotors. A lightweight battery cell packaging approach is developed for gram-scale mAABs, which has only < 10 wt% of the packaging overhead. The mAAB cell is engineered for powering a commercial small-scale quadrotor, demonstrating a 3-fold energy density improvement over the required flight power threshold for the HS190 commercial small-scale quadrotor. The mAAB has also demonstrated an inaugural flight with a notable increase in flight duration using a customized 3D printed small-scale quadrotor platform, with a 13.1-minute flight time compared to a 4.5 min flight time for a commercial mLIB. This work underscores the potential of mAABs to substantially extend operational durations of small-scale quadrotors.

Materials and methods

mAAB materials and assembly

High purity aluminum foils (purity > 99.99%) with thicknesses of 100, 200, and 500 micrometers are obtained from Thermo Fisher and Laurand Associates. These foils are precisely cut and shaped using aviation snips and a 1 mm hole punch cutter. The cut Al foils are then flattened by a hydraulic press to re-planarize any edge deformation from the cutting and punching process. Following the pressing process, the samples undergo sonicator cleaning to remove any surface contaminants or impurities. This cleaning process involves three 15-minute rounds using the following solvents in sequence: distilled water, ethyl alcohol, and acetone. After cleaning, the aluminum foil anodes are dried at 70 °C for 4 h. Potassium hydroxide (99.99% purity, Sigma-Aldrich) and sodium stannate trihydrate (96% purity, Thermo Fisher) are used for electrolyte preparation. Unless otherwise specified, freshly prepared electrolyte was used within 2 h of preparation. The cathode comprises platinum-based carbon cloth (4 $\frac{mg}{cm^2}$ Platinum Black - Carbon Cloth Electrode, Fuel Cell Store), which is trimmed to the required size using a hollow punch. The mAAB cell body frame is fabricated using a Creality Ender-3 S1 filament 3D printer. The filament used is polypropylene with a 1.75 mm diameter FL105PP Natural Color from Braskem Company. High

temperature epoxy (J-B Weld High Heat Epoxy Syringe, Dark Grey) is used to attach the anode and the cathode to the PP body frame.

mAAB testing and characterization

30 gauge Cu wire (99.9% Purity, Craftwire USA) is used to electrically connect the mAAB to external components such as potentiostats and small-scale quadrotors. Cu wires are wrapped on aluminum anode foil handles and attached to the surfaces of carbon cloth cathodes. The connections between the copper wires and both the cathode and anode materials are coated with silver paste (2spi) for enhanced electrical connection. Three-electrode tests are carried out using a Gamry 600 Potentiostat, with a platinum electrode as the counter electrode and a Hg/HgO reference electrode. The power and discharge performance tests are conducted using a Rigol DL3021 DC load. In the power performance test, the current was scanned from 0 to 2.5 A at a rate of 0.5 A/sec, with a cutoff voltage of 0.4 V. Given that corrosion can also occur during battery storage, electrolyte is introduced immediately prior to battery use. This approach effectively limits aluminum corrosion before the battery becomes operational, ensuring optimal anode utilization and preserving the energy density for discharge. In all testing, electrolytes are preheated to 60 $^{\circ}C$, which are then injected to the cell using plastic syringes. The small-scale quadrotor body frame is fabricated using a Formlabs 3 + resin 3D printer with High Temp resin (Formlabs). The battery is attached to the 3D-printed small-scale quadrotor platform using the high temperature epoxy. During the flight duration measurement, the RF controller of the HS190 is used to maintain the small-scale quadrotor in the same lateral and vertical position to the largest extent possible. The duration for which the small-scale quadrotor remains airborne is defined as the flight duration. The reported battery mass in this study refers to the mass before testing. During discharge, the battery mass may increase due to aluminum oxidation reaction, but the magnitude is small (around 5% of the total mass in the battery) and does not significantly affect packaging design or cell structure optimization.

Data availability

All data needed to evaluate the conclusions in the paper are available in the main text or the Supplementary Materials.

Received: 20 July 2025; Accepted: 8 October 2025
Published online: 23 December 2025

References

1. Ahmad, A., Ordoñez, J., Cartujo, P. & Martos, V. Remotely piloted aircraft (RPA) in agriculture: A pursuit of sustainability', Jan. 01. *MDPI AG*. https://doi.org/10.3390/agronomy11010007 (2020).
2. Mohsan, S. A. H., Khan, M. A., Noor, F., Ullah, I. & Alsharif, M. H. 'Towards the Unmanned Aerial Vehicles (UAVs): A Comprehensive Review', Jun. 01, 2022, *MDPI*. https://doi.org/10.3390/drones6060147
3. Kagan, C. R., Arnold, D. P., Allen, M. G. & Olsson, R. H. 'IoT4Ag: MEMS-Enabled Distributed Sensing, Communications, and Information Systems for the Internet of Things for Precision Agriculture', in *Proceedings of the IEEE International Conference on Micro Electro Mechanical Systems (MEMS)*, Institute of Electrical and Electronics Engineers Inc., Jan. pp. 350–353. (2021). https://doi.org/10.1109/MEMS51782.2021.9375346
4. Mohsan, S. A. H., Othman, N. Q. H., Li, Y., Alsharif, M. H. & Khan, M. A. Unmanned aerial vehicles (UAVs): practical aspects, applications, open challenges, security issues, and future trends', Mar. 01. *Springer Sci. Bus. Media Deutschland GmbH*. https://doi.org/10.1007/s11370-022-00452-4 (2023).
5. Floreano, D. & Wood, R. J. 'Science, technology and the future of small autonomous drones', May 27, 2015. *Nature Publishing Group* https://doi.org/10.1038/nature14542
6. Huang, Y., Lyu, H., Allen, M. G. & Allen, S. A. B. 'Extended Flight Duration Small-Scale Quadrotors Powered by High-energy-density High-power-density Micro Aluminum-air Batteries', in *Solid-State Sensor, Actuator, and Microsystems Workshop (Hilton Head 2024)*, May (2024).
7. Korchenko, A. G. & Illyash, O. S. 'The generalized classification of unmanned air vehicles', in *IEEE 2nd International Conference Actual Problems of Unmanned Air Vehicles Developments Proceedings (APUAVD)*, IEEE, 2013, pp. 28–34., IEEE, 2013, pp. 28–34. (2013).
8. Huang, Y., Vyletel, J., Allen, M. G. & Allen, S. A. B. 'Microfabrication-Enhanced Carbon Fiber Cathodes for High Discharge Rate Aluminum-Air Batteries', in *21st International Conference on Micro and Nanotechnology for Power Generation and Energy Conversion Applications (PowerMEMS)*, IEEE, 2022, pp. 195–197., IEEE, 2022, pp. 195–197. (2022).
9. Zhang, J. et al. High-energy-density zinc–air microbatteries with lean PVA–KOH–K2CO3 gel electrolytes. *ACS Appl. Mater. Interfaces*. **15** (5), 6807–6816 (2023).
10. Venkatesh, V. et al. Zinc film anodes for air microbatteries: fabrication, approaches, and utilization optimization. *J. Micromech. Microeng.* **33** (5), 055001 (2023).
11. Itani, K., De Bernardinis, A. & 'Review on New-Generation Batteries Technologies. : Trends and Future Directions', Nov. 01, 2023, *Multidisciplinary Digital Publishing Institute (MDPI)*. https://doi.org/10.3390/en16227530
12. Jafferis, N. T., Helbling, E. F., Karpelson, M. & Wood, R. J. 'Untethered flight of an insect-sized flapping-wing microscale aerial vehicle', *Nature*, vol. 570, no. 7762, pp. 491–495, Jun. (2019). https://doi.org/10.1038/s41586-019-1322-0
13. Boukoberine, M. N., Zhou, Z. & Benbouzid, M. 'Power Supply Architectures for Drones - A Review', in *IECON Proceedings (Industrial Electronics Conference)*, IEEE Computer Society, Oct. pp. 5826–5831. (2019). https://doi.org/10.1109/IECON.2019.8927702
14. Mulgaonkar, Y. et al. 'Power and weight considerations in small, agile quadrotors', in Micro-and Nanotechnology Sensors, Systems, and Applications VI, SPIE, 376–391. (2014).
15. https://www.lithium-polymer-batteries.com/
16. Stux, A. & Swider-Lyons, K. 'Survey of commercial small lithium polymer batteries'. *Chemical Dynamics Diagnostics Branch*, (2007).
17. https://www.tdk-electronics.tdk.com/download/2427688/a88e3aeab8be00d00fce586b0efec694/06-dl-ceracharge-presentation.pdf
18. https://www.digikey.com/en/products/detail/stmicroelectronics/EFL1K0AF39RL/7702470
19. https://www.digikey.com/en/products/detail/stmicroelectronics/EFL700A39-RL/4869276
20. Yue, X. et al. A nearly Packaging-Free design paradigm for Light, Powerful, and Energy-Dense primary microbatteries. *Adv. Mater.* **33** (35), 2101760 (2021).

21. Choudhury, S. et al. Solid-state polymer electrolytes for high-performance lithium metal batteries. *Nat. Commun.* **10** (1). https://doi.org/10.1038/s41467-019-12423-y (Dec. 2019).
22. Fan, X. & Wang, C. 'High-voltage liquid electrolytes for Li batteries: Progress and perspectives', Sep. 21, *Royal Society of Chemistry*. (2021). https://doi.org/10.1039/d1cs00450f
23. Kwade, A. et al. Current status and challenges for automotive battery production technologies. *Nat. Energy*. **3** (4), 290–300 (2018).
24. Coppola, M., McGuire, K. N., De Wagter, C. & De Croon, G. C. H. E. A survey on swarming with micro air vehicles: fundamental challenges and constraints. *Front. Robot AI*. **7**, 18 (2020).
25. Ahn, H., Kim, D., Lee, M. & Nam, K. W. 'Challenges and possibilities for aqueous battery systems'. *Dec. 01 2023 Springer Nature* https://doi.org/10.1038/s43246-023-00367-2
26. Zhao, Q. et al. 'Electrolytes for aluminum-air batteries: advances, challenges, and applications', Feb. 10, *Royal Society of Chemistry*. (2023). https://doi.org/10.1039/d2se01744j
27. Li, Y. & Lu, J. Metal–air batteries: will they be the future electrochemical energy storage device of choice? *ACS Energy Lett.* **2** (6), 1370–1377 (2017).
28. Andre, D. et al. Future generations of cathode materials: an automotive industry perspective. *J. Mater. Chem. Mater.* **3** (13), 6709–6732 (2015).
29. Zheng, J. et al. 'Understanding thermodynamic and kinetic contributions in expanding the stability window of aqueous electrolytes', *Chem*, vol. 4, no. 12, pp. 2872–2882, (2018).
30. Chen, J., Naveed, A., Nuli, Y., Yang, J. & Wang, J. Designing an intrinsically safe organic electrolyte for rechargeable batteries. *Energy Storage Mater.* **31**, 382–400 (2020).
31. Hammami, A., Raymond, N. & Armand, M. Runaway risk of forming toxic compounds. *Nature* **424** (6949), 635–636 (2003).
32. Goel, P., Dobhal, D. & Sharma, R. C. 'Aluminum–air batteries: A viability review', Apr. 01, *Elsevier Ltd*. (2020). https://doi.org/10.1016/j.est.2020.101287
33. Mori, R. 'Recent Developments for Aluminum–Air Batteries', Jun. 01, *Springer Science and Business Media B.V.* (2020). https://doi.org/10.1007/s41918-020-00065-4
34. Wu, S. et al. Oct., 'Hybrid high-concentration electrolyte significantly strengthens the practicability of alkaline aluminum-air battery', *Energy Storage Mater*, vol. 31, pp. 310–317, (2020). https://doi.org/10.1016/j.ensm.2020.06.024
35. Naidoo, Y., Stopforth, R. & Bright, G. 'Development of an UAV for search & rescue applications', in *IEEE Africon'11*, IEEE, pp. 1–6. (2011).
36. Park, S. & Choi, Y. 'Applications of unmanned aerial vehicles in mining from exploration to reclamation: A review', *Minerals*, vol. 10, no. 8, p. 663, (2020).
37. Lyu, M., Zhao, Y., Huang, C. & Huang, H. Unmanned aerial vehicles for search and rescue: A survey. *Remote Sens. (Basel)*. **15** (13), 3266 (2023).
38. Huang, Y. et al. 'Cost-Effective Microfabricated Silver-Based Paper Cathodes for High-Discharge-Rate Aluminum-Air Batteries', in *Electrochemical Society Meeting Abstracts 245*, The Electrochemical Society, Inc., p. 2113. (2024).
39. Liu, Y. et al. 'A comprehensive review on recent progress in aluminum–air batteries', Jul. 01, 2017. *KeAi Publishing Commun. Ltd* https://doi.org/10.1016/j.gee.2017.06.006
40. Huang, Y. 'MEMS-Based Electrochemical Power Sources for Extended Operational Duration of Micro Unmanned Vehicles', PhD Dissertation, University of Pennsylvania, (2024).
41. Huang, Y., Lyu, H., Allen, M. G. & Bidstrup Allen, S. A. 'High-Energy-Density High-Power-Density Micro Aluminum-Air Batteries for Small Scale Quadcopters', in *Electrochemical Society Meeting Abstracts 245*, The Electrochemical Society, Inc., p. 52. (2024).
42. Macdonald, D. D. & English, C. Development of anodes for aluminium/air batteries—solution phase Inhibition of corrosion. *J. Appl. Electrochem.* **20**, 405–417 (1990).
43. Kundu, A., Mallick, S., Ghora, S. & Raj, C. R. 'Advanced Oxygen Electrocatalyst for Air-Breathing Electrode in Zn-Air Batteries', Sep. 01, *American Chemical Society*. (2021). https://doi.org/10.1021/acsami.1c08462
44. Cheng, F. & Chen, J. Metal–air batteries: from oxygen reduction electrochemistry to cathode catalysts. *Chem. Soc. Rev.* **41** (6), 2172–2192. https://doi.org/10.1039/c1cs15228a (Feb. 2012).
45. Huang, Y. et al. Mechanistic study of hydroxide ion consumption in ultralean PVA hydrogel electrolytes for High-Energy-Density micro Zinc-Air batteries. *J. Electrochem. Soc.* **170** (10), 100523 (2023).
46. Lim, J. H. et al. 'Importance of hydroxide ion conductivity measurement for alkaline water electrolysis membranes', *Membranes (Basel)*, vol. 12, no. 6, p. 556, (2022).
47. Faegh, E., Ng, B., Hayman, D. & Mustain, W. E. Practical assessment of the performance of aluminium battery technologies. *Nat. Energy*. **6** (1), 21–29 (2021).
48. Dougherty, T. A., Karpinski, A. P., Lapp, S. P., Kallok, R. N. & Natale, S. V. 'Aluminum-air reserve power unit for use in a 6 kW standby power system', in *Proceedings of INTELEC 95. 17th International Telecommunications Energy Conference*, IEEE, pp. 821–827. (1995).
49. Ilyukhina, A. V., Kleymenov, B. V. & Zhuk, A. Z. Development and study of aluminum-air electrochemical generator and its main components. *J. Power Sources*. **342**, 741–749 (2017).
50. Cameron, K. & Kowalenko, V. 'Portable unmanned aircraft system concept investigation', (1995).
51. Egan, D. *Development and Characterisation of a Lightweight Alkaline aluminium-air Cell* (University of Southampton, 2015).

Author contributions

Y.H., M.G.A., and S.A.B.A. designed the research; Y.H., C.W., H.L. performed the research; Y.H., M.G.A., and S.A.B.A. wrote the paper.

Funding

This work was carried out in part at the singh center for nanotechnology, which is supported by the nsf national nanotechnology coordinated infrastructure program under grant no. Nnci-2025608. This material is based upon work supported in part by the iot4ag engineering research center funded by the national science foundation (nsf) under nsf cooperative agreement number eec-1941529. Any opinions, findings and conclusions, or recommendations expressed in this material are those of the author(s), and do not necessarily reflect those of the nsf.

Declarations

Competing interests

The authors declare no competing interests.

Conflict of interest
The authors declare no competing interests.

Additional information
Supplementary Information The online version contains supplementary material available at https://doi.org/10.1038/s41598-025-23776-4.

Correspondence and requests for materials should be addressed to Y.H., M.G.A. or S.A.B.A.

Reprints and permissions information is available at www.nature.com/reprints.

Publisher's note Springer Nature remains neutral with regard to jurisdictional claims in published maps and institutional affiliations.